

Article

# Relationship between Casing Pressure and Non-Synchronous Vibration in an Axial Compressor <sup>†</sup>

Valerie Hernley <sup>1,\*</sup>, Aleksandar Jemcov <sup>1</sup>, Jeongseek Kang <sup>1</sup>, Matthew Montgomery <sup>2</sup> and Scott C. Morris <sup>1,\*</sup>

<sup>1</sup> Notre Dame Turbomachinery Laboratory, Department of Mechanical and Aerospace Engineering, University of Notre Dame, South Bend, IN 46637, USA; ajemcov@nd.edu (A.J.); jkang6@nd.edu (J.K.)

<sup>2</sup> Doosan Enerbility, Palm Beach Gardens, FL 33418, USA; matthew.montgomery@doosan.com

\* Correspondence: vhernley23@gmail.com (V.H.); smorris1@nd.edu (S.C.M.)

<sup>†</sup> This paper is an extended version of our paper published in Proceedings of the 16th International Symposium on Unsteady Aerodynamics, Aeroacoustics and Aeroelasticity of Turbomachines, Toledo, Spain, 19–23 September 2022; paper No. ISUAAAT16-26.

**Abstract:** The relationship between aerodynamic forcing and non-synchronous vibration (NSV) in axial compressors remains difficult to ascertain from experimental measurements. In this work, the relationship between casing pressure and blade vibration was investigated using experimental observations from a 1.5-stage axial compressor under off-design conditions. The wavenumber-dependent auto-spectral density (ASD) of casing pressure was introduced to aid in understanding the characteristics of pressure fluctuations that lead to the aeromechanical response. Specifically, the rotor blade's natural frequencies and nodal diameters could be directly compared with the pressure spectra. This analysis indicated that the rotating disturbances coincided with the first bending (1B) and second bending (2B) vibration modes at certain frequencies and wavenumbers. The non-intrusive stress measurement system (NSMS) data showed elevated vibration amplitudes for the coincident nodal diameters. The amplitude of the wavenumber-dependent pressure spectra was projected onto the single-degree-of-freedom (SDOF) transfer function and was compared with the measured vibration amplitude. The results showed a near-linear relationship between the pressure and vibration data.

**Keywords:** compressor; non-synchronous vibration; convective NSV; rotating instabilities; pre-stall disturbances



**Citation:** Hernley, V.; Jemcov, A.; Kang, J.; Montgomery, M.; Morris, S.C. Relationship between Casing Pressure and Non-Synchronous Vibration in an Axial Compressor. *Int. J. Turbomach. Propuls. Power* **2024**, *9*, 14. <https://doi.org/10.3390/ijtp9020014>

Academic Editors: Damian Vogt and Roque Corral

Received: 20 October 2023

Revised: 25 February 2024

Accepted: 5 March 2024

Published: 2 April 2024



**Copyright:** © 2024 by the authors. Licensee MDPI, Basel, Switzerland. This article is an open access article distributed under the terms and conditions of the Creative Commons Attribution (CC BY-NC-ND) license (<https://creativecommons.org/licenses/by-nc-nd/4.0/>).

## 1. Introduction

Non-synchronous vibration (NSV) in axial compressors can be caused by a variety of physical mechanisms. One commonly occurring mechanism is NSV caused by pre-stall rotating pressure disturbances [1]. Other terms used to describe these phenomena include “rotating instabilities” [2,3] and “convective NSV” [4]. The characteristics of these pre-stall disturbances and how they relate to blade vibration remain poorly understood. Experimentally, characterizing the rotating disturbances relies heavily on unsteady casing pressure measurements. The present work examines the relationship between casing pressure measurements and non-synchronous blade vibration in a 1.5-stage axial compressor under off-design conditions where rotating disturbances were present.

While the physical mechanisms of pre-stall rotating disturbances remain poorly understood, the defining characteristics are fairly ubiquitous throughout the literature. Pre-stall disturbances tend to occur around half of the blade-passing frequency and are similar to rotating stall in that they propagate circumferentially at a fraction of the rotor speed [2,5–9]. In the early literature, this phenomenon was referred to as “rotating instabilities” [2,3,10]. For example, Kameier and Neise observed distinct peaks superimposed on a broadband hump around half of the blade-passing frequency (BPF) in the casing pressure spectrum [2]. Baumgartner et al. showed that the separation distance of the peaks corresponded to the propagation speed of the disturbances [3]. Since these early works, these distinct

spectral characteristics have been used to identify pre-stall disturbances in pressure spectra [1,6–12]. In particular, Mailach et al. [10] showed a stair-step pattern of aerodynamic circumferential wavenumber versus frequency, consistent with observations from other authors that each frequency peak or “band” was associated with a different circumferential wavenumber [1,5,8,13].

There have been many examples in the literature of pre-stall rotating disturbances causing non-synchronous vibration [4,7,8,11,14]. In general, it is helpful to examine relationships between aerodynamic forcing and blade vibration using modal coordinates. If all of the blades are identical (no mistuning), then the modal deflections are independent and the governing equation for each mode is that of a linear single-degree-of-freedom (SDOF) harmonic oscillator [15–18]:

$$\ddot{z}_{pq}(t) + 2\zeta_{pq}\omega_{pq}\dot{z}_{pq}(t) + \omega_{pq}^2 z_{pq}(t) = f_{pq}(t), \quad (1)$$

where  $z_{pq}(t)$  is the modal deflection of the structural vibration mode with natural frequency  $\omega_{pq}$  and damping ratio  $\zeta_{pq}$ , given that  $p$  indicates the nodal diameter and  $q$  the mode family [18,19]. The forcing in modal coordinates,  $f_{pq}$ , is given by an area integral of the unsteady pressure on the blade multiplied by the blade-alone mode shape, including a (spatial) discrete Fourier transform to take into account the nodal diameter [17,18,20,21]:

$$f_{pq}(t) = \sum_{j=0}^{N-1} e^{-\frac{2\pi i j p}{N}} \int \Delta P(j, s, t) \psi_{pq}(s) ds, \quad (2)$$

where  $\Delta P(j, s, t)$  denotes the (unsteady) pressure difference between the pressure and suction sides of blade  $j$  at spatial coordinate  $s$ .

The unsteady pressure,  $\Delta P(j, s, t)$ , is extremely difficult to measure experimentally. Thus, casing pressure measurements are often analyzed in an attempt to understand the aerodynamic forcing that leads to non-synchronous vibration. For example, using casing pressure measurements, several authors have shown that resonant forcing of a vibration mode was only possible if (1) the structural nodal diameter and aerodynamic circumferential wavenumber were the same and (2) the frequency of the aerodynamic fluctuations was close to the vibration mode’s natural frequency [3,8].

One of the challenges in characterizing pre-stall disturbances and the ensuing blade vibration is that the physics are inherently stochastic. Day [6] observed the pre-stall disturbances to be “small in circumferential extent, rotate at about half rotor speed in the same direction, have a high circumferential count, and are always changing in intensity, wavenumber, and frequency.” This constantly changing nature was observed by Brandstetter et al. [7], who showed that the disturbance size-per-blade-passage and counter-per-revolution oscillated stochastically. Given the stochastic nature of the aerodynamic forcing, it is helpful to consider statistics of both the forcing and vibration response. In particular, the auto-spectral density (ASD) is a helpful statistic as it allows for relationships to be expressed in the frequency domain. Taking the ASD of Equation (1) shows that the ASD of the modal displacement  $z_{pq}(t)$ ,  $S_{zz}(\omega)$  is linearly related to the ASD of the modal force  $f_{pq}(t)$ ,  $S_{ff}(\omega)$ , by [22–24]

$$S_{zz}(\omega) = |G(\omega)|^2 S_{ff}(\omega), \quad (3)$$

where

$$|G(\omega)|^2 = \frac{1}{\left(\omega_{pq}^2 - \omega^2\right)^2 + \left(2\zeta_{pq}\omega_{pq}\omega\right)^2} \quad (4)$$

is the squared magnitude of the SDOF transfer function for the vibration mode with natural frequency  $\omega_{pq}$  and damping ratio  $\zeta_{pq}$  [22,23,25]. In general, the physics of the pre-stall disturbances affect the spectral characteristics of the modal force ASD,  $S_{ff}(\omega)$ . Furthermore, Equation (3) shows that the vibration response,  $S_{zz}(\omega)$ , scales linearly with the amplitude of the modal force.

Previously, Hernley et al. [14] showed that the comparison of Equations (3) and (4) with measured spectral characteristics can allow the identification of a forced response versus flutter. The objective of the present work was to study the relationship between the respective amplitudes of the unsteady casing pressure and blade vibration during forced-response NSV. In particular, NSV was observed with varied mass flow rates along a part-speed characteristic in a 1.5-stage power generation compressor.

This paper is organized in the following manner. Section 2 provides a brief description of the experimental setup. Section 3 shows the experimental casing pressure and blade vibration results at various mass flow rates along the compressor characteristic. In Section 4, the relationship between pressure and vibration amplitudes is investigated. Finally, Section 5 summarizes and discusses the main conclusions of this work.

## 2. Experimental Methods

Experiments were conducted in a 10 MW compressor rig at the Notre Dame Turbomachinery Lab (NDTL). A schematic of the facility is shown in Figure 1a. The compressor was operated in an open-loop configuration: atmospheric air entered the facility through the inlet, was redirected axially by upstream turning vanes, and flowed through the inlet settling chamber where perforated plates and wire meshes straightened the incoming flow. It was then directed through a bellmouth into the test article section, after which it was directed through an exit valve (throttle) to be exhausted back to the atmosphere. The exit valve was opened or closed to adjust the mass flow rate through the facility. The test article was rotated by a shaft connected to the 10 MW motor through a gearbox and torquemeter. The gearbox increased the rotational speed from the motor to the test article by a gear ratio of approximately 11. The shaft speed was adjustable by the motor's variable speed drive.

The test article was a 1.5-stage power generation compressor designed for aeromechanic studies. The 1.5-stage compressor consisted of a variable inlet guide vane (IGV) (64 vanes), a rotor (32 blades), and a stator (42 vanes). The rotor was a low hub-to-tip ratio transonic compressor with a diameter of approximately 0.6 m. The compressor design was a bladed disk with dovetail attachments. Upstream of the rotor, a variable IGV was opened or closed to adjust the incidence angle of the flow entering the rotor. For all of the results presented in this paper, the IGV was partially closed compared to the design value. Additionally, the operating conditions presented in this work were from a part-speed condition with a rotor tip Mach number of about 0.7.

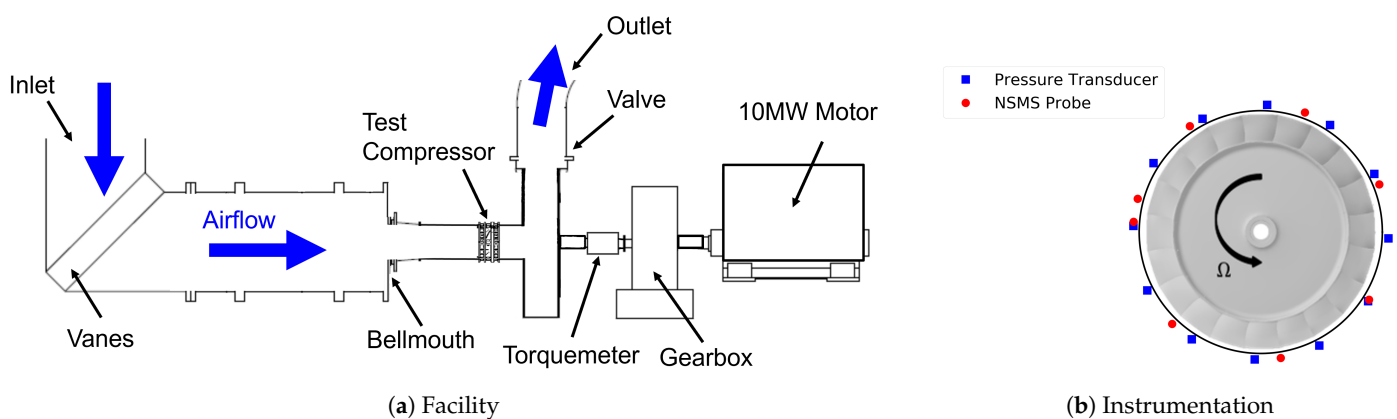


**Figure 1.** (a) Schematic of the 10 MW compressor rig at the Notre Dame Turbomachinery Lab. (b) Schematic of unsteady pressure and blade vibration instrumentation, where blue squares indicate 12 equally spaced pressure transducers (XTL-190(M) Kulites) at 5% axial chord upstream of the rotor leading edge and red circles indicate 8 non-equally spaced non-intrusive stress measurement system (NSMS) probes at the rotor leading edge.

Performance measurements such as stage total-to-total pressure ratio, total-to-total temperature ratio, and efficiency were obtained at each operating point. Total pressures and

total temperatures were measured from Kiel-head probe rakes located at the inlet struts just upstream of the IGV and at the stage outlet location just downstream of the stator trailing edge. Additionally, the mass flow rate was measured by the calibrated bellmouth, and the shaft rate was measured by a tachometer, which allowed the performance measurements to be obtained as a function of the corrected mass flow rate and corrected speed.

Experimental measurements of unsteady pressure and compressor blade vibration were obtained to study the aeromechanics of the compressor. The measurements were obtained with instrumentation mounted to the rotor casing, as shown schematically by Figure 1b, which shows the rotor casing represented by a solid black circle. Note that the compressor shown in Figure 1b is a schematic and not representative of the hardware used. A circumferential array of 12 fast-response pressure transducers (XTL-190(M) Kulites, Kulite Semiconductor Products, Inc., Leonia, NJ, USA) was arranged in the rotor casing at an axial position of 5% rotor chord upstream of the rotor leading edge, as shown schematically by the blue squares in Figure 1b. The 12 pressure transducers were equally spaced, each separated by 30 degrees, and had a sampling frequency of 150 kHz. Additionally, blade vibration was monitored using blade tip timing via a non-intrusive stress measurement system (NSMS). Eight non-equally spaced NSMS probes (Agilis spot light probe, AMS001164-36, Agilis Measurement Systems, Inc., Palm Beach Gardens, FL, USA) were mounted to the rotor casing just aft of the rotor blade leading edge, as shown by the red circles in Figure 1b. Each NSMS probe had an effective sampling frequency of  $N$  per rev, where  $N$  was the number of rotor blades. Least-squares methods were used to determine which mode was vibrating and its corresponding modal amplitude [26].

### 3. Experimental Results

The steady performance results of the part-speed, IGV-partially-closed compressor characteristic are considered. Figure 2 shows the experimental results of the compressor total pressure ratio (PR) as a function of the corrected mass flow rate, where all values have been normalized by the full-speed, aerodynamic design point value. Two experiments were conducted. First, transient data were obtained, where the facility throttle valve was closed in a continuous manner over a period of 110 s. Second, steady measurements were obtained at eleven discrete throttle positions along the characteristic.

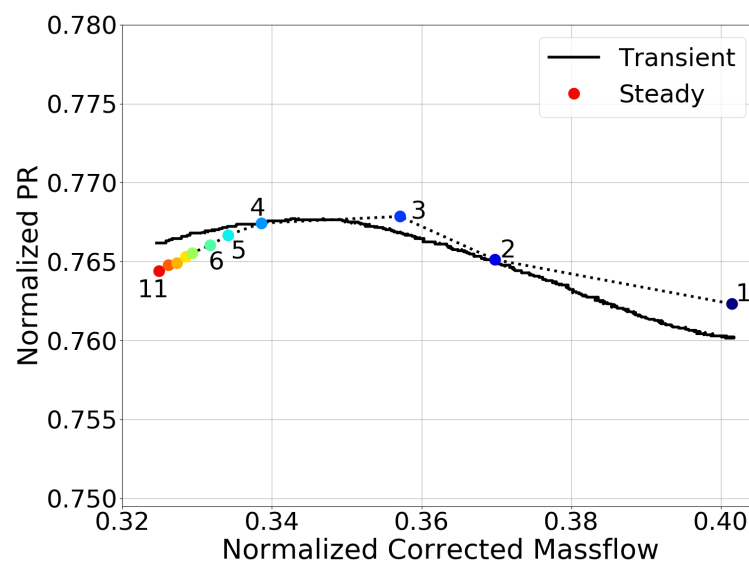


**Figure 2.** Compressor characteristic showing total-to-total pressure ratio (PR) versus corrected mass flow for a part-speed, IGV-partially-closed operating condition, as measured by a throttle transient experiment (black) and throttle steady-state experiments (colored circles). All values were normalized by the full-speed design point values.

The results from the transient experiment are shown by the black line. The throttle was initially fully open, corresponding to a normalized corrected mass flow rate of approximately 0.4. The throttle was continuously closed until high-amplitude 1B blade vibration was observed, which resulted in the emergency valve of the facility being opened when the normalized corrected mass flow was approximately 0.33. The results from the steady experiments are shown by the eleven points in Figure 2. The points have been color-coded such that operating point 1 (OP1) in dark blue corresponds to the largest mass flow rate, and operating point 11 (OP11) in red corresponds to the lowest mass flow rate.

It is interesting to note that over the entire range of this constant-speed characteristic, the efficiency values (not shown here) were approximately 50–55%. Therefore, these experiments represent an extremely off-design operating condition. However, power generation compressors are required to operate in this regime as they are powered on and off; therefore, even under these off-design conditions, it is important to understand the aerodynamic forcing and how it relates to blade vibration. In the following sections, the transient results will be discussed first, followed by a detailed analysis of the steady operating points.

### 3.1. Transient Results

The transient casing pressure characteristics are useful for investigating the physics of the aerodynamic forcing. In particular, the literature has shown that rotating disturbances and other unsteady flow physics relevant to blade vibration are recognizable in the auto-spectral density (ASD) results from a single casing pressure transducer [2,3,9,11,27]. Motivated by this, Figure 3 shows the auto-spectral density (ASD),  $\phi(f)$ , from a single leading-edge casing pressure transducer during the transient experiment (black line from Figure 2). The ASD was computed using moving windows of 0.002 s with 50% overlap, where each window was divided into 30 blocks for Welch's method of block averaging [28]. The amplitude of the ASD was plotted on a logarithmic scale (color contours) versus time on the abscissa and frequency on the ordinate. All frequency values were normalized by shaft rate to be expressed as an engine order (EO), and the frequency resolution was approximately 0.1 EO. In addition, time on the abscissa was shifted so that 0 s corresponded to the opening of the throttle valve at the end of the transient. The entire transient was 110 s, but only 70 s are shown for ease of visualization. The vertical white lines near  $-60$  and  $-22$  s represent a pause in data acquisition necessary to save the data files and restart the acquisition. Along the top of Figure 3, the steady operating points that had the same corrected mass flow rate as certain times in the transient are labeled, which will be useful for comparison between steady and transient results.

The transient experiment began with the fully open throttle; thus, the initial part of the transient ( $-110$  to  $-55$  s) indicated very low levels of pressure fluctuations. The only exception was the blade-passing frequency (BPF) indicated by the dark red line at 32 EO. From  $-55$  to  $-25$  s, discrete bands of unsteady pressure fluctuations around half of the BPF (8–16 EO) were observed, similar to what Kameier and Neise called “rotating instability” [2]. The spacing between the different bands was approximately 0.65 EO. This value approximates the circumferential propagation speed as a fraction of rotor speed [2,5]. It will be shown in the following section that each of these peaks corresponded to a different circumferential wavenumber. The frequencies of each band increased slightly as the mass flow was reduced, while the spacing between the different bands remained approximately constant. From  $-25$  to  $-15$  s, the mid-frequency content shifted to slightly higher frequencies, and the discrete bands were no longer as pronounced.

At approximately  $-10$  s, low-frequency content appeared in the 0–8 EO range. Again, distinct bands were visible, separated by about 0.55 EO. It will be shown in the following section that each of these bands also corresponded to a different circumferential wavenumber. Similar bands were observed as an upper sideband to the BPF, at the same frequencies relative to the BPF as the low-frequency values. During this time, the mid-frequency amplitude decreased and became more broadband. At 0 s, the rig emergency valve was opened, rapidly decreasing unsteady pressure at all frequencies below the BPF.

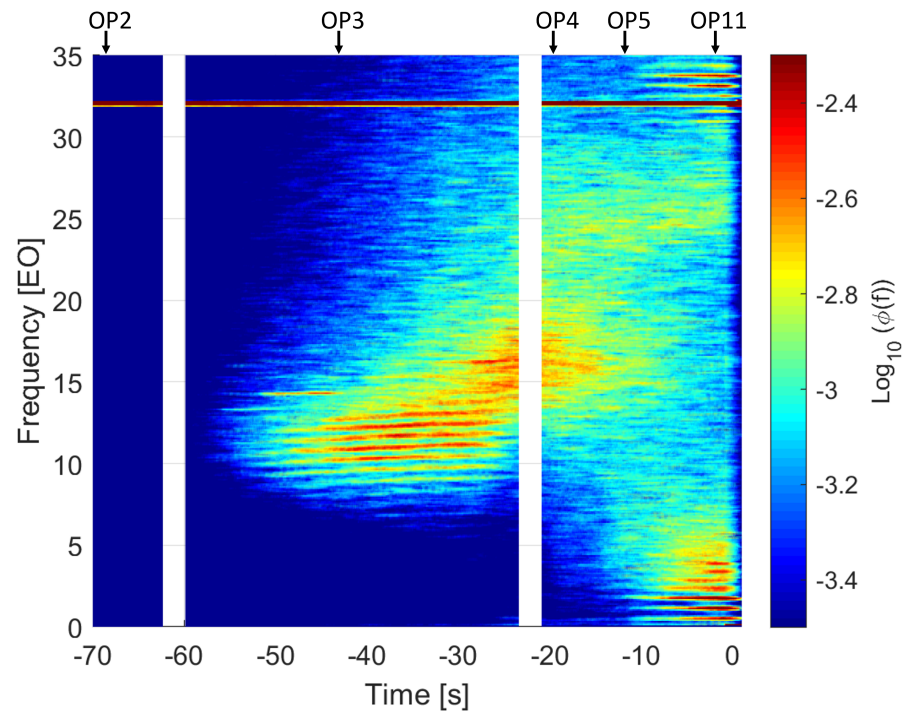


**Figure 3.** Leading-edge casing unsteady pressure ASD,  $\phi(f)$ , during the throttle transient computed using moving windows of 0.002 s with 50% overlap. Numbers at the top correspond to steady experiments with the same corrected mass flow rate as a given time in the transient (Figure 2).

The blade vibration amplitudes during the transient experiment are now considered. Figure 4 shows the vibration amplitude versus time measured by NSMS probes during the transient experiment. For clarity, only the nodal diameters with the highest amplitude vibration are shown: for the 1B mode (Figure 4a),  $p = -8, -7$ , and  $-6$ , and for the 2B mode (Figure 4b),  $p = 7, 8, 9$ , and  $10$ . As with the pressure data, the numbers on the top denote the corresponding steady-state operating points. Additionally, time on the abscissa has been shifted such that 0 s corresponds to the opening of the emergency valve.

First, the instantaneous amplitudes for the 1B mode are considered (Figure 4a). At the beginning of the transient, from  $-110$  to  $-55$  s, no significant 1B vibration was present. From  $-55$  to  $-25$  s, the amplitude of all 1B nodal diameters increased slightly to around 0.18 mm. From  $-25$  to  $-15$  s, the amplitude of all modes decreased to a negligible value. Then, from  $-10$  to 0 s, the  $p = -7$  amplitude increased sharply to a maximum value of around 0.62 mm. The  $p = -6$  and  $p = -8$  nodal diameters also increased in amplitude from  $-10$  to 0 s but had a lower maximum amplitude of about 0.4 mm and 0.25 mm, respectively.

The instantaneous amplitudes for the 2B mode are shown in Figure 4b. Overall, the 2B mode had lower amplitudes than the 1B mode, as is visible by noting the different ordinate scales between Figure 4a,b. For the 2B mode, the nodal diameter with the highest instantaneous vibration amplitude changed as the mass flow rate was reduced throughout the transient. At the beginning of the transient experiment, all 2B vibration amplitudes were low. Then, around  $-55$  s, the 2B,  $p = 10$  nodal diameter grew in amplitude to a value around 0.08 mm. From  $-48$  to  $-42$  s, the  $p = 9$  nodal diameter grew above the  $p = 10$  response and reached a maximum amplitude of approximately 0.15 mm. Then, from  $-40$  to  $-30$  s, the  $p = 8$  nodal diameter had the highest instantaneous amplitude. However, this value was lower than the  $p = 9$  response of the previous time segment, reaching a maximum amplitude of approximately 0.12 mm for the  $p = 8$  nodal diameter. Subsequently, from  $-30$  to  $-20$  s, the  $p = 7$  nodal diameter had the highest instantaneous amplitude, reaching a maximum value of 0.21 mm, the highest of all the 2B mode ampli-

tudes throughout the transient. Finally, towards the end of the transient, from  $-20$  to  $0$  s, all 2B nodal diameters decreased in amplitude as the mass flow rate was further reduced.

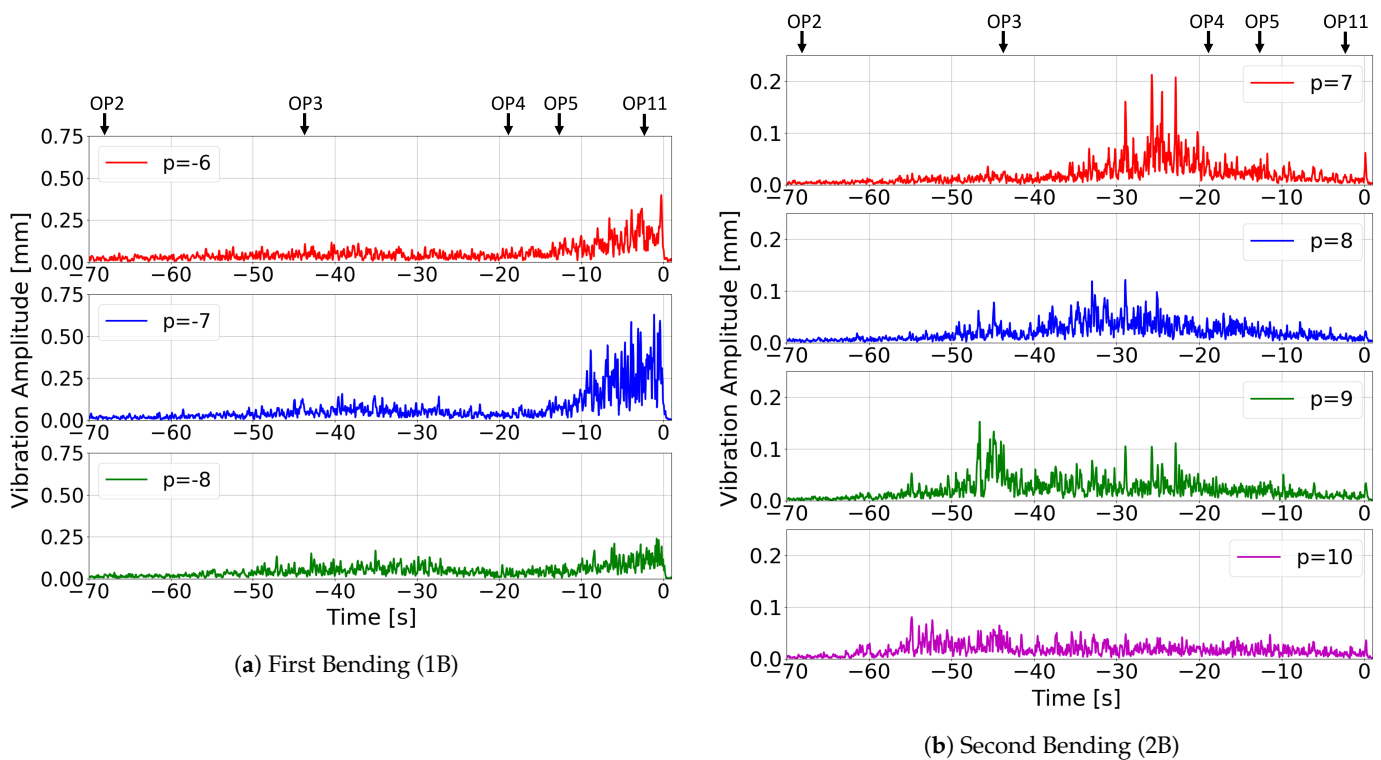


**Figure 4.** Instantaneous vibration amplitudes measured by NSMS during the transient experiment for mode families (a) 1B and (b) 2B for the nodal diameters,  $p$ , with the highest amplitude vibration. Numbers at the top correspond to steady experiments with the same corrected mass flow rate as a given time in the transient (Figure 2).

The vibration data can now be considered in the context of the pressure data presented in Figure 3. In both Figures 3 and 4, there were two regions of interest: (1)  $-55$  to  $-15$  s and (2)  $-10$  to  $0$  s. From  $-55$  to  $-15$  s, the unsteady pressure showed distinct bands around half of the BPF. In this same time segment, the 1B vibration amplitudes increased slightly for all nodal diameters, and the 2B vibration amplitudes increased significantly. Additionally, which 2B nodal diameter had the highest amplitude at a given instant changed throughout this time segment. In the region from  $-10$  to  $0$  s, additional unsteady pressure fluctuations appeared at low frequencies ( $0$ – $7$  EO), which also showed distinct bands indicative of rotating disturbances. In this time segment, there was a sharp increase in the 1B,  $p = -7$  vibration amplitude, and some increase in the 1B  $p = -6$  and  $-8$  amplitudes. There was a decrease in the 2B vibration amplitudes during this time period. Qualitatively, for both modes, the vibration amplitudes observed in Figure 4 scaled with the amplitude of the pressure disturbances observed in Figure 3.

### 3.2. Steady Results

The relationship between the unsteady casing pressure and blade vibration was further investigated using steady operating conditions. Eleven steady operating conditions were obtained, and approximately 20 s of data were acquired at each operating condition. The results from a single steady operating point are presented first, followed by results from all remaining operating points.

Vibration temporal characteristics are useful for understanding forcing mechanisms [11,18]. However, the vibration data shown in Figure 4 had temporal characteristics that were affected by both the unsteady aerodynamics and the transient boundary conditions of the experiment, i.e., the throttle closure rate. For example, it was unclear

whether the growth of the 1B,  $p = -7$  vibration amplitude in Figure 4a was due to a forced response, where the magnitude of the aerodynamic forcing grew as the throttle was closed, or whether the vibration response was an exponential growth characteristic of a linear instability (i.e., flutter). Therefore, the temporal characteristics at steady operating conditions provide greater insight into the underlying physics. Figure 5 shows a time segment of the instantaneous vibration amplitude for (a) the 1B,  $p = -7$  mode at OP11 and (b) the 2B,  $p = 9$  mode at OP3. The time series for each nodal diameter was achieved via a least-squares fit of the NSMS data using standard techniques in Agilis' commercial software [26]. For both modes, the instantaneous amplitude grew and decayed in an intermittent, stochastic manner. This intermittency was characterized by statistics such as the vibration amplitude's mean and standard deviation, where the mean was visualized by the horizontal black line in Figure 5. For example, the 1B,  $p = -7$  mode in Figure 5a had a mean amplitude of 0.34 mm and a standard deviation of 0.165 mm. The 2B,  $p = 9$  mode in Figure 5b had a mean value of 0.078 mm and a standard deviation of 0.0385 mm. For both modes, the coefficient of variation, defined as the standard deviation divided by the mean, was approximately 0.47. The coefficient of variation was approximately 0.47 for all nodal diameters at all steady operating points, indicating that similar, intermittent vibration amplitudes characterized each nodal diameter and operating point. It is known theoretically that an SDOF system forced by white noise has a vibration response amplitude that oscillates stochastically [19,23,24]. Extending this to the steady vibration data in Figure 5, the observed stochastic amplitude modulation was likely indicative of stochastic aerodynamic forcing.

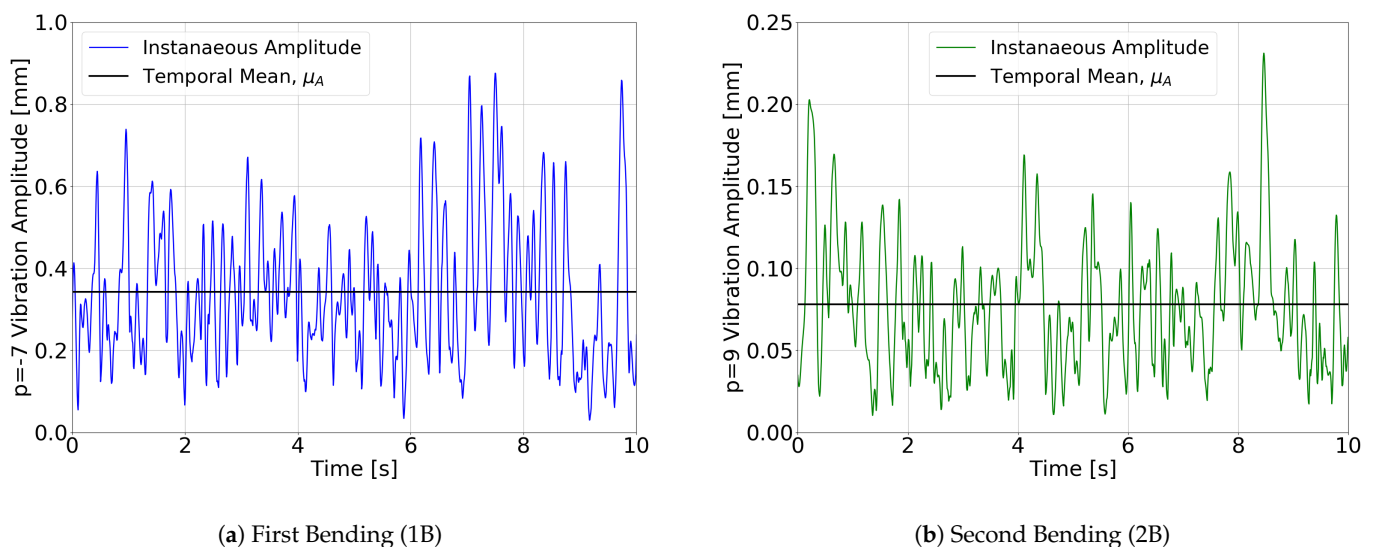


**Figure 5.** Vibration amplitude measured by NSMS for (a) 1B,  $p = -7$  and (b) 2B,  $p = 9$  at steady operating points (a) OP11 and (b) OP3, respectively.

To study vibration for each nodal diameter and operating point, the stochastic vibration response was characterized by the temporal mean, as was demonstrated by the black line in Figure 5. Figure 6 shows the mean vibration amplitude versus the nodal diameter for each of the 11 steady operating points. For clarity, only the range of nodal diameters with the highest amplitude vibration is shown: (a) 1B,  $p = -11$  through  $-5$  and (b) 2B,  $p = 5$  to 11.

For the 1B mode in Figure 6a, all nodal diameters from  $p = -5$  to  $p = -11$  increased in amplitude monotonically as the compressor mass flow rate was reduced from OP1 to OP11. The only exception was that the vibration amplitudes for OP3 were slightly higher than OP4 for nodal diameters  $-6$  to  $-10$ . At OP5, the  $p = -6$  and  $p = -7$  nodal diameters had similar amplitudes around a mean value of 0.1 mm. At OP6, the  $p = -7$  nodal diameter had the highest amplitude, and from OP7 to OP11,  $p = -7$  grew monotonically as the mass

flow rate was reduced, reaching a maximum of 0.35 mm at OP11. Nodal diameters  $p = -6$  and  $p = -8$  also had moderately high amplitudes and demonstrated a clear monotonic increase with the operating point.

For the 2B mode in Figure 6b, the shape of the curve (i.e., which nodal diameter had the highest amplitude vibration) differed for the various operating points. At OP3,  $p = 9$  had the highest amplitude of 0.08 mm, while  $p = 8$  and 10 also had elevated amplitudes. Then, at OP4,  $p = 7$  had the highest amplitude vibration, around 0.065 mm, which was lower than the  $p = 9$  amplitude from OP3. As the mass flow rate was further reduced, all 2B vibration amplitudes decreased slightly. Still, the shape of the curve remained similar to OP4, with nodal diameters  $p = 7$  or 6 having the highest amplitude vibration. By OP11, the amplitude was around 0.04 mm for all nodal diameters, approximately half of the maximum amplitude at OP3.

The results from the steady experiments were consistent with the transient results from Figure 4. Direct comparison of amplitudes was not feasible because of the intermittency: Figure 4 shows instantaneous amplitudes while Figure 6 shows mean amplitudes. However, in both the transient and steady results, the 1B,  $p = 7$  mode had the highest amplitude vibration at low mass flow rates. Additionally, the 2B amplitudes were elevated at moderate mass flow rates (in the middle of the part-speed characteristic), but the nodal diameter that had the highest amplitude vibration changed as the mass flow rate was reduced. For example, OP3 corresponded to approximately  $-43$  s in the transient, when the 2B,  $p = 9$  mode had the highest amplitude vibration. In addition, OP4 corresponded to  $-18$  s in the transient, when the 2B,  $p = 7$  mode was higher than the other nodal diameters. Steady-state OP3 and OP4 were significantly different in terms of mass flow rate. The transient results in Figure 4 indicated elevated amplitudes for  $p = 8$  at mass flow rates between OP3 and OP4. Thus, it could be speculated that, had steady-state measurements been acquired at this intermediate-mass flow rate, Figure 6b would have shown a continuous trend from  $p = 9$  to 8 to 7 as the mass flow rate was reduced.

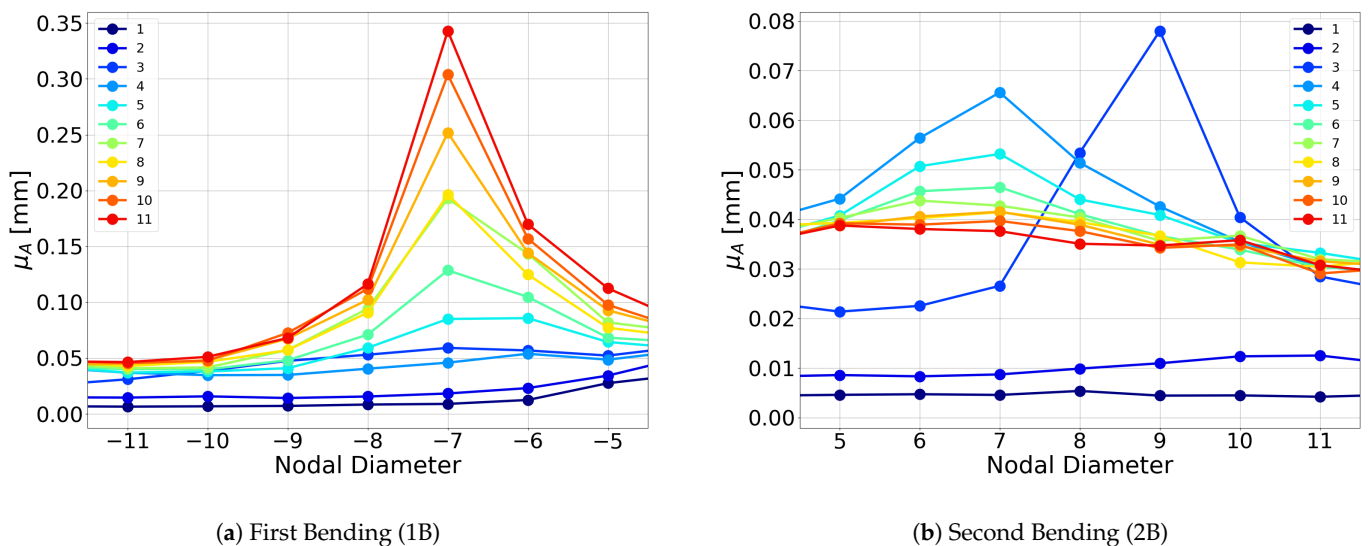


**Figure 6.** Mean vibration amplitude,  $\mu_A$ , measured by NSMS for mode families (a) 1B and (b) 2B. Colors correspond to the 11 steady operating points shown in Figure 2.

The casing pressure data at the steady operating conditions are now considered. Since data from 12 pressure transducers were available, it was helpful to analyze both the frequency and circumferential wavenumber characteristics of the casing pressure. The pressure fluctuations were first expressed as a function of the discrete circumferential wavenumber,  $k$ , by computing the Fourier Series coefficients as:

$$a_k(t) = \frac{1}{M} \sum_{m=0}^{M-1} P(\theta^m, t) e^{-\frac{2\pi i k m}{M}}, \quad (5)$$

where  $P(\theta^m, t)$  was the signal from the  $m^{\text{th}}$  pressure transducer in the circumferential array of  $M = 12$  equally spaced transducers. To analyze frequency content, the auto-spectral density function was then computed from each of these (complex-valued) Fourier coefficients,  $a_k(t)$ , defined as [22,23,29]

$$\phi_k(f) = \lim_{T \rightarrow \infty} \frac{2\pi}{T} \mathbb{E}[\tilde{a}_k(f) \tilde{a}_k^*(f)], \quad (6)$$

where  $\tilde{a}_k(f)$  was the (temporal) discrete Fourier transform of the complex conjugate of  $a_k(t)$ . The sign convention was chosen such that a forward traveling wave in the lab reference frame corresponded to positive  $k$  and positive  $f$ . As in the previous section, Welch's method [28] of block averaging was employed. Thus, the wavenumber-dependent ASD,  $\phi_k(f)$ , characterized the casing pressure's average frequency and circumferential wavenumber attributes.

The wavenumber-dependent ASD of casing pressure can now be considered in tandem with the vibration eigenmodes. This was motivated by studies that have shown that it is important to compare both the frequency and the circumferential wavenumber of the aerodynamics to the natural frequency and nodal diameter of the vibration mode [3,8,14]. Vibration modes can be overlaid on a contour plot of  $\phi_k(f)$  using the relationship [14,19]

$$p = -k + cN, \quad f^S = k - f^R, \quad (7)$$

where  $p$  indicates the structural nodal diameter,  $k$  indicates the aerodynamic circumferential wavenumber, and  $c$  represents a Fourier aliasing constant due to a continuous pressure field being projected onto  $N$  discrete blades (Equation (1)). The frequency  $f^S$  indicates the vibration's natural frequency in the lab reference frame, while  $f^R$  is the natural frequency defined in the rotor's reference frame, both in units of EO. Under this part-speed operating condition, the 1B mode had a natural frequency of  $f^R = 3.145$  EO, and the 2B mode had a natural frequency of  $f^R = 8.75$  EO. These frequencies were predicted with finite-element analysis and were consistent with the values observed experimentally in the NSMS data. Physically, Equation (7) arises from the change in the reference frame between the vibration modes expressed in the rotor's reference frame and pressure data measured in the lab reference frame. Additionally, the aliasing can occur because aerodynamic wavenumbers,  $k$ , can range from  $-\infty$  to  $\infty$  due to the continuous pressure field, while structural nodal diameters are limited to  $N$  due to the discrete number of blades.

Contours of the casing pressure spectra,  $\phi_k(f)$ , are shown in Figure 7 with circumferential wavenumber  $k$  on the ordinate and frequency on the abscissa, where the frequency resolution was approximately 0.01 EO. Since there were 12 pressure transducers, only 12 independent wavenumbers could be computed; however, the data were repeated on the ordinate for visualization of the higher, aliased wavenumbers. This repetition allowed for visual identification of diagonal trends in  $\phi_k(f)$ , the slope of which could be interpreted as the propagation speed of rotating disturbances [3]. The red circles in Figure 7 indicate the 1B vibration mode for various nodal diameters, while the red squares indicate the 2B vibration mode. Nodal diameters corresponding to the highest amplitude response (Figures 4 and 6) are indicated by the red arrows. Since speed was constant, the vibration modes had the same frequencies across all steady operating points. However, the pressure data changed relative to these vibration modes as the mass flow rate was reduced from OP1 to OP11, as shown by Figure 7a–f.

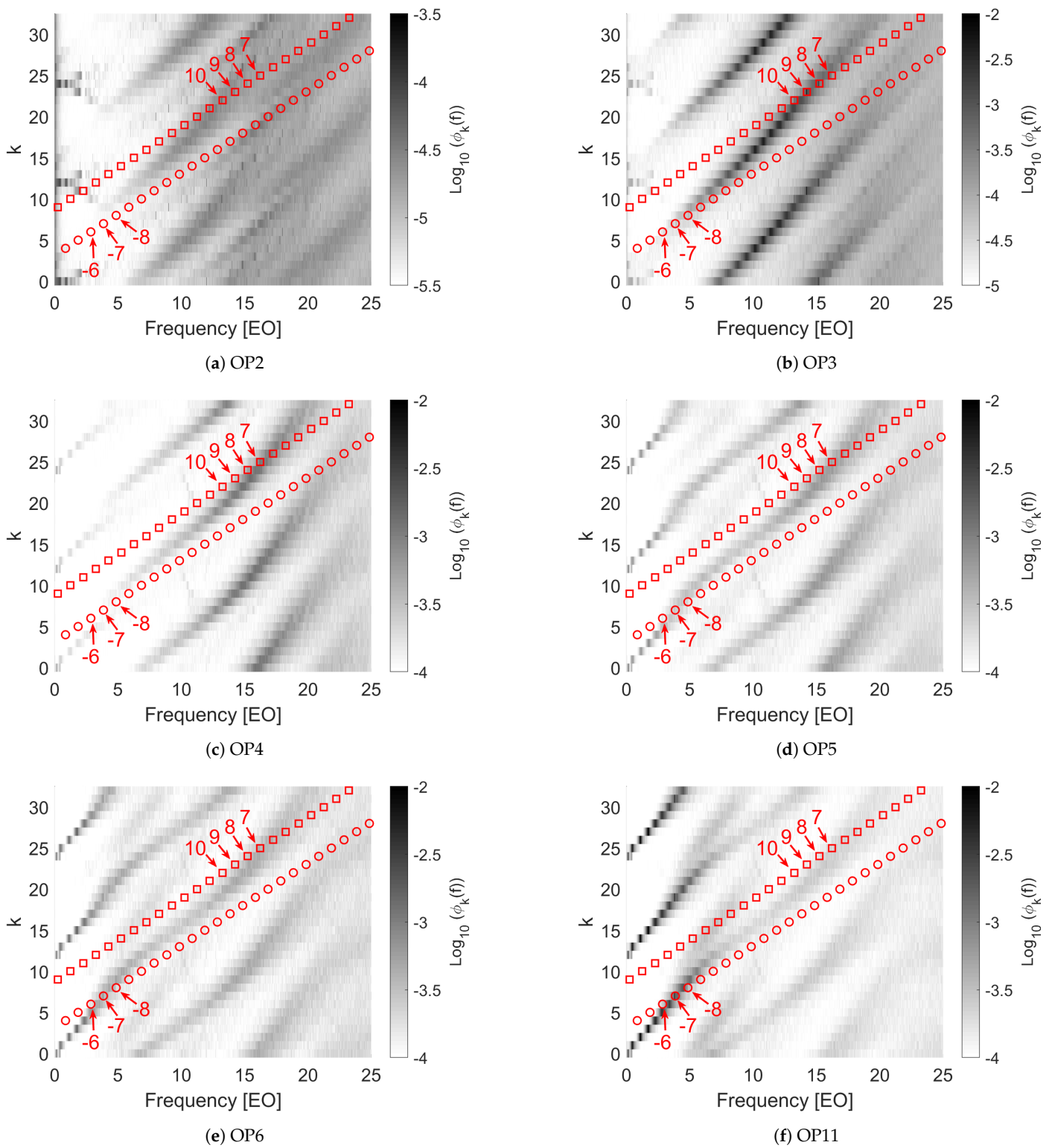


**Figure 7.** Contour plot of the casing pressure wavenumber-dependent ASD,  $\phi_k(f)$ , for select steady operating points. Vibration modes overlaid via Equation (7) are shown by the red circles (1B) and red squares (2B), and red arrows indicate select nodal diameters for each mode.

Operating point 2, shown in Figure 7a, resulted in low-amplitude, broadband pressure fluctuations from around 10–25 EO. Several distinct groups of diagonal lines were visible, with a slope ranging from 0.5 to 0.8. These diagonal regions of local maxima were

interpreted to be rotating pressure fluctuations traveling circumferentially at a fraction of the shaft rate.

At OP3, in Figure 7b, the pressure local maxima formed a single diagonal with a slope of 0.62. This diagonal region spanned frequencies from 8 to 15 EO and wavenumbers from 10 to 32, forming a “stairstep pattern” that the literature has identified as a key characteristic of pre-stall rotating disturbances, or “rotating instabilities” [1,2,5,10,13]. These higher wavenumbers,  $k = 10\text{--}32$ , were assumed to be physically relevant compared to the fundamental  $k = 0\text{--}11$  based on the fact that rotating disturbances are known to propagate at a speed around half of the rotor speed [2,5–9].

In Figure 7b, the diagonal of pressure local maxima intersected the 1B vibration mode (red circles) at aerodynamic wavenumbers of  $k = 7$  to 10, corresponding to structural nodal diameters  $-7$  to  $-10$ , respectively. Additionally, the local maxima at higher frequencies intersected the 2B vibration mode (squares) at aerodynamic wavenumbers  $k = 21$  to 25. These wavenumbers corresponded to structural nodal diameters  $+11$  to  $+7$ , respectively, given a Fourier aliasing constant of  $c = 1$  with 32 rotor blades in Equation (7). As shown in Figure 6, OP3 showed elevated vibration amplitudes for the nodal diameters intersected by the rotating pressure disturbances. In particular, the 2B mode had the highest amplitude vibration for nodal diameter  $+9$ , which was directly intersected by the diagonal region of rotating pressure fluctuations at wavenumber  $k = 23$  in Figure 7b.

At OP4, shown in Figure 7c, the local maxima shifted to higher frequencies and wavenumbers, but a coherent diagonal region indicative of rotating disturbances was still present. The highest amplitude pressure fluctuations occurred from 12 to 20 EO and  $k = 15$  to 32. This shift to higher frequencies at OP4 compared to OP3 was consistent with the transient data in Figure 3: the mid-frequency pressure fluctuations shifted to higher frequencies as the mass flow rate of the compressor was reduced. Although Figure 3 shows less pronounced “banding” from 12 to 20 EO at  $-18$  s, the steady results in Figure 7c indicate that the stair-step pattern between frequency and wavenumber was still present at this lower mass flow operating point. Considering the vibration modes, the shift of the pressure fluctuations to higher frequencies caused the intersection with the 2B mode to occur primarily at nodal diameter 7 ( $k = 25$ ). As shown in Figure 6, OP4 had the highest 2B vibration amplitude at  $p = 7$ . Furthermore, both the pressure and vibration data showed lower amplitudes at OP4 than at OP3. Additionally, OP4 in Figure 7c indicated low-amplitude, low-frequency, and low-wavenumber content with a slope around 0.7. These were interpreted as low-frequency rotating pressure fluctuations distinct from the mid-frequency disturbances.

At OP5, shown in Figure 7d, the amplitude of the low-frequency (0–5 EO) pressure fluctuations increased, and the amplitude of the mid-frequency (12–20 EO) pressure fluctuations decreased slightly such that the two regions had a similar amplitude. The slope of the local maxima in the 0–5 EO region decreased to a value of approximately 0.55. The decreased speed of the low-frequency fluctuations resulted in an intersection with the 1B vibration mode, predominantly at nodal diameter  $-7$ . In Figure 6a, OP5 showed elevated vibration amplitudes for the 1B mode at nodal diameters  $-7$  and  $-6$ . Additionally, for the mid-frequency pressure fluctuations in Figure 7d, the slope of the maxima from 12 to 20 EO remained approximately the same, but the amplitude of the maxima decreased compared to OP4. Thus, the intersection with the 2B vibration mode occurred at the same nodal diameters, but, as seen in Figure 6b, the 2B vibration amplitudes were lower at OP5 compared to OP4.

At OP6, shown in Figure 7e, the low-frequency rotating disturbances grew in amplitude. Still, the range of frequencies, wavenumbers, and the slope of the local maxima remained the same. In fact, from OP 7 to 11 (only OP11 is shown here in Figure 7f), the  $k - f$  characteristics remained the same, but the amplitude of the low-frequency pressure disturbances grew monotonically with the operating point (i.e., decreasing mass flow rate). Comparatively, the 1B vibration data in Figure 6a indicated that at OP6, the  $p = -7$  nodal diameter began to have the highest amplitude. Then, from OP6 to OP11, the 1B

vibration amplitudes grew monotonically, particularly for nodal diameters  $-6$ ,  $-7$ , and  $-8$ , with the highest amplitudes occurring for  $p = -7$ . In contrast, the mid-frequency rotating pressure disturbances decreased in amplitude monotonically from OP6 to OP11, and Figure 6b shows that the 2B vibration amplitudes for nodal diameters 6 through 9 also decreased monotonically.

Overall, the qualitative relationship between casing pressure and vibration amplitudes was evident by comparing Figure 7 to Figure 6. For both the 1B and 2B vibration modes, elevated vibration amplitudes for certain nodal diameters occurred when the diagonal regions of high-amplitude pressure fluctuations were coincident with the vibration mode in both frequency and wavenumber (i.e., “intersections” in Figure 7). These coherent diagonal regions of pressure fluctuations were physically indicative of pre-stall rotating disturbances. Hernley showed that pre-stall disturbances’ frequency and wavenumber characteristics were affected by physical parameters such as their propagation speed, size, and frequency of occurrence [19]. Thus, the speed, size, and frequency of occurrence of pre-stall disturbances affect which, if any, vibration modes are forced on resonance. Furthermore, comparing Figure 7 to Figure 6 showed that when the pre-stall disturbances forced a mode on resonance, the amplitude of the vibration scaled with the amplitude of the pressure fluctuations. A more precise comparison of pressure and vibration amplitudes is discussed in the following section.

#### 4. Relationship between Pressure and Vibration

Given the results of Figures 6 and 7, examining the relationship between pressure and vibration amplitudes is of interest. Equations (1) and (3) indicate that it would be appropriate to project the pressure spectra onto the SDOF transfer function. The SDOF-projected pressure amplitude was defined as

$$\tilde{p}^2 \equiv \frac{A_b^2}{2\pi} \int_{\omega_1}^{\omega_2} |G(\omega)|^2 \phi_k(\omega) d\omega, \quad (8)$$

where  $\phi_k(\omega)$  was the wavenumber-dependent ASD of the casing pressure transducers and  $|G(\omega)|^2$  was the squared magnitude of the SDOF transfer function for a given  $pq$  vibration mode. The integration bounds were defined as  $\omega_1 = \Omega(f^S - 0.5)$  and  $\omega_2 = \Omega(f^S + 0.5)$ , given  $f^S$  was the vibration mode’s natural frequency in the lab reference frame (Equation (7)) and  $\Omega$  was the shaft angular frequency. These limits were chosen because, for a lightly-damped mode,  $|G(\omega)|^2$  is extremely peaked around the mode’s natural frequency, and the amplitude of the forcing spectrum in the frequency range around the natural frequency has the greatest effect on the vibration response [23]. Additionally, Equation (8) includes the scaling constant of the blade area,  $A_b$ , to approximate the modal force integral given by Equation (1). This scaling constant also allows  $\tilde{P}$  to have units of mm and thus be directly compared to vibration amplitudes.

The SDOF-projected pressure amplitude can now be compared to the measured vibration amplitudes. Figure 8 shows the mean vibration amplitude,  $\mu_A$ , measured by NSMS (Figure 6) versus the SDOF-projected pressure amplitude measured by the casing pressure transducers, as defined by Equation (8). Each color corresponds to a different nodal diameter, and the individual data points for each nodal diameter include the 11 steady operating conditions. The 1B mode, shown in Figure 8a, indicated a near-linear trend for all nodal diameters. The slope of this linear trend was similar for nodal diameters  $-7$  through  $-11$  but was slightly higher for nodal diameters  $-5$  and  $-6$ . The 2B mode in Figure 8 also showed a near-linear trend, and all nodal diameters had a similar slope. Therefore, for both vibration modes, Figure 8 demonstrates a near-linear relationship between casing pressure spectral amplitudes and vibration amplitudes.

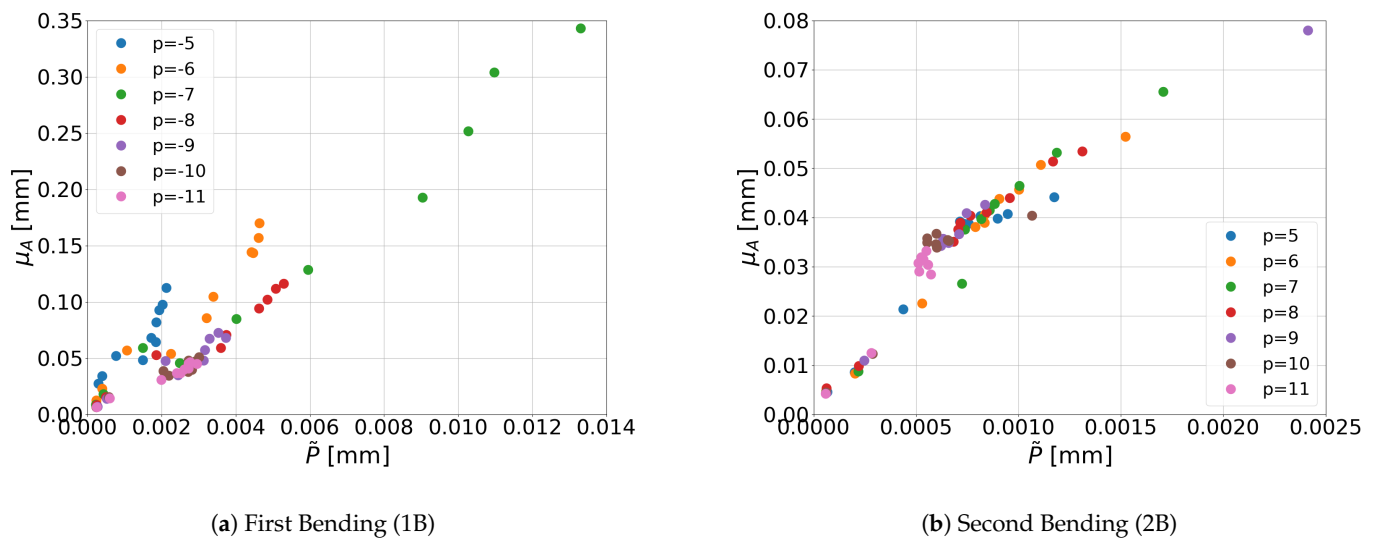


**Figure 8.** Scatter plot of mean vibration amplitude from NSMS,  $\mu_A$ , versus the SDOF-projected pressure amplitude,  $\tilde{P}$  (Equation (8)), for each of the 11 steady operating points. Colors correspond to different nodal diameters,  $p$ , for mode families (a) 1B and (b) 2B.

## 5. Conclusions

Non-synchronous vibration was observed under off-design conditions in an axial compressor. Under these off-design conditions, casing pressure measurements indicated two types of pre-stall rotating disturbances: mid-frequency disturbances around half of the blade-passing frequency (similar to observations from [2,3,6,10]), and low-frequency rotating disturbances with a similar diagonal trend in wavenumber and frequency. The compressor operating condition affected the wavenumber and frequency characteristics of the pre-stall rotating disturbances. As speed was held constant and mass flow rate was reduced, the mid-frequency disturbances moved to higher frequencies and wavenumbers. As the mass flow rate was further reduced, the mid-frequency disturbances decreased in amplitude, but the low-frequency disturbances appeared and grew in amplitude. The mid-frequency disturbances forced specific nodal diameters of the 2B vibration mode, while the low-frequency disturbances forced the 1B vibration mode primarily at nodal diameter  $-7$ .

The time series representation of blade vibration indicated a highly stochastic amplitude. It is known that rotating disturbances are stochastic in nature [6,7], and the stochastic amplitude modulation observed in the steady vibration data (Figure 5) was indicative of stochastic aerodynamic forcing. These results demonstrated that the non-synchronous vibration was caused by stochastic, rotating pressure disturbances forcing certain modes on resonance.

The introduction of the wavenumber-dependent ASD of the casing pressure data allowed for a direct comparison between aerodynamic frequencies and wavenumbers and vibration natural frequencies and nodal diameters, respectively. This comparison was achieved by overlaying vibration modes on a contour plot of  $\phi_k(f)$ , as demonstrated in Figure 7. It was observed that when the rotating pressure disturbances were coincident with a vibration mode in both frequency and wavenumber, high-amplitude vibration occurred. Therefore, the analysis method introduced in Figure 7 may be used for NSV in a way that is analogous to how the Campbell diagram is used for synchronous vibration.

A direct assessment of the relationship between casing pressure fluctuations and blade vibration was obtained by considering the SDOF-projected amplitude of  $\phi_k(f)$ ,  $\tilde{P}$ . Qualitatively, the collapse of the data in Figure 8 provided strong evidence that the unsteady aerodynamics of the compressor had a direct, causal link to the blade vibration amplitudes. Specifically, the mathematical background given by Equation (3) indicated that modal amplitudes scale linearly with the amplitude of the modal force. When the modal

force is stochastic in nature, as is the case with rotating pressure fluctuations, the linear relationship is best expressed in terms of an ASD (Equations (3)). The near-linear nature of measured vibration amplitudes relative to the wavenumber-dependent ASD of casing pressure suggests that casing pressure measurements capture essential characteristics of the actual modal pressure force on the blades (compare Equation (8) to Equations (2)–(4)). This has implications for how both component test data and measurements in engines might be interpreted. For example, single-point pressure measurements (as shown in Figure 3) are typical but alone do not provide an understanding of how those fluctuations may affect blade vibration. The circumferential wavenumber is a key characteristic that allows casing pressure measurements to be related to blade vibration. Naturally, the quantitative assessment of vibration relative to  $\tilde{P}$  will require future studies to understand the impact of compressor geometry and operating parameters.

**Author Contributions:** Conceptualization, V.H., A.J., J.K., M.M. and S.C.M.; methodology, V.H., M.M. and S.C.M.; formal analysis, V.H.; investigation, J.K.; resources, J.K., M.M. and S.C.M.; writing—original draft preparation, V.H.; writing—review and editing, A.J. and S.C.M.; visualization, V.H.; funding acquisition, V.H. All authors have read and agreed to the published version of the manuscript.

**Funding:** This research was funded by the National Defence Science and Engineering Graduate Fellowship Program (NDSEG).

**Data Availability Statement:** Data is contained within the article.

**Acknowledgments:** The authors would like to thank Doosan Enerbility for providing the test article, technical advice, and permission to publish.

**Conflicts of Interest:** Author Matthew Montgomery was employed by the company Doosan Enerbility. The remaining authors declare that the research was conducted in the absence of any commercial or financial relationships that could be construed as a potential conflict of interest.

## Nomenclature

The following nomenclature are used in this manuscript:

$c$	integer describing Fourier aliasing
$f$	frequency
$f^S$	natural frequency in the stationary (lab) reference frame
$f^R$	natural frequency in rotor's reference frame
$i$	imaginary unit, $\sqrt{-1}$
$j$	blade number index
$k$	aerodynamic circumferential wavenumber
$N$	number of rotor blades
$P$	pressure
$\tilde{P}$	SDOF-projected pressure amplitude
$p$	nodal diameter
$q$	mode family index
$T$	period
$t$	time
$z_{pq}$	modal displacement
1B	first bending mode family
2B	second bending mode family
ASD	auto-spectral density
BPF	blade-passing frequency
EO	engine order (frequency normalized by shaft rate)
NSMS	non-intrusive stress measurement system
NSV	non-synchronous vibration
SDOF	single degree of freedom
OP	operating point
$\zeta_{pq}$	structural damping coefficient of $pq^{th}$ vibration mode
$\theta$	circumferential (azimuthal) coordinate

$\mu_A$	mean vibration amplitude
$\phi$	ASD of casing pressure
$\Omega$	shaft rate
$\omega$	angular frequency
$\omega_{pq}$	natural frequency of $pq^{th}$ vibration mode
$\mathbb{E}$	expectation operator
*	complex conjugate

## References

- de Almeida, V.B.C.; Tüzüner, E.; Eck, M.; Peitsch, D. Numerical Characterization of Prestall Disturbances in a Compressor Stage. In Proceedings of the Turbo Expo: Power for Land, Sea, and Air, Boston, MA, USA, 26–30 June 2023. [\[CrossRef\]](#)
- Kameier, F.; Neise, W. Rotating Blade Flow Instability as a Source of Noise in Axial Turbomachines. *J. Sound Vib.* **1997**, *203*, 833–853. [\[CrossRef\]](#)
- Baumgartner, M.; Kameier, F.; Hourmouziadis, J. Non-Engine Order Blade Vibration in a High Pressure Compressor. In Proceedings of the Twelfth International Symposium on Airbreathing Engines, Melbourne, Australia, 10–15 September 1995.
- Stapelfeldt, S.; Brandstetter, C. Non-synchronous Vibration in Axial Compressors: Lock-in Mechanism and Semi-analytical Model. *J. Sound Vib.* **2020**, *488*, 115649. [\[CrossRef\]](#)
- Dodds, J.; Vahdati, M. Rotating Stall Observations in a High Speed Compressor: Part 1—Experimental Study. In Proceedings of the ASME Turbo Expo 2014: Turbine Technical Conference and Exposition, Düsseldorf, Germany, 16–20 June 2014. [\[CrossRef\]](#)
- Day, I.J. Stall, Surge, and 75 Years of Research. *J. Turbomach.* **2015**, *138*, 011001. [\[CrossRef\]](#)
- Brandstetter, C.; Jüngst, M.; Schiffer, H.P. Measurements of Radial Vortices, Spill Forward, and Vortex Breakdown in a Transonic Compressor. *J. Turbomach.* **2018**, *140*, 061004. [\[CrossRef\]](#)
- Möller, D.; Schiffer, H.P. On the Mechanism of Spike Stall Inception and Near Stall Nonsynchronous Vibration in an Axial Compressor. *J. Eng. Gas Turbines Power* **2021**, *143*, 021007. [\[CrossRef\]](#)
- Brandstetter, C.; Ottavy, X.; Paoletti, B.; Stapelfeldt, S. Interpretation of Stall Precursor Signatures. *J. Turbomach.* **2021**, *143*, 121011. [\[CrossRef\]](#)
- Mailach, R.; Lehmann, I.; Vogeler, K. Rotating Instabilities in an Axial Compressor Originating from the Fluctuating Blade Tip Vortex. *J. Turbomach.* **2001**, *123*, 453–460. [\[CrossRef\]](#)
- Holzinger, F.; Wartzek, F.; Jüngst, M.; Schiffer, H.P.; Leichtfuss, S. Self-Excited Blade Vibration Experimentally Investigated in Transonic Compressors: Rotating Instabilities and Flutter. *J. Turbomach.* **2016**, *138*, 041006. [\[CrossRef\]](#)
- Flete, X.; Binder, N.; Bousquet, Y.; Cros, S. Numerical Investigation of Rotating Instability Development in a Wide Tip Gap Centrifugal Compressor. *Int. J. Turbomach. Propuls. Power* **2023**, *8*, 25. [\[CrossRef\]](#)
- D’Antonio, J.P. Front Stage Axial Compressor Stable Rotating Stall: An Experimental Investigation of Pressure Field Spatial and Temporal Scales. Ph.D. Thesis, University of Notre Dame, Notre Dame, IN, USA, 2015.
- Hernley, V.; Kang, J.; Montgomery, M.; Chung, J.H.; Jemcov, A.; Morris, S.C. Identification of Compressor Vibration Aerodynamic Forcing Mechanisms by Spectral Characteristics. *J. Eng. Gas Turbines Power* **2023**, *146*, 051008. [\[CrossRef\]](#)
- Lane, F. System Mode Shapes in the Flutter of Compressor Blade Rows. *J. Aeronaut. Sci.* **1956**, *23*, 54–66. [\[CrossRef\]](#)
- Crawley, E. Aeroelastic Formulation for Tuned and Mistuned Rotors. In *AGARD Manual on Aeroelasticity in Axial-Flow Turbomachines—Chapter 19: Structural Dynamics and Aeroelasticity*; Technical Report AGARD-AG-298; AGARD: Neuilly sur Seine, France, 1988; Volume 2.
- Olson, B.J.; Shaw, S.W.; Shi, C.; Pierre, C.; Parker, R.G. Circulant matrices and their application to vibration analysis. *Appl. Mech. Rev.* **2014**, *66*, 040803. [\[CrossRef\]](#)
- Hernley, V.; Jemcov, A.; Morris, S.C. Aerodynamic Forcing Models for Compressor Aeromechanics. In Proceedings of the Turbo Expo: Power for Land, Sea, and Air, Rotterdam, The Netherlands, 13–17 June 2022.
- Hernley, V.L. Identification of Aerodynamic Forcing Mechanisms from Experimental Measurements of Compressor Blade Vibration. Ph.D. Thesis, University of Notre Dame, Notre Dame, IN, USA, 2023. [\[CrossRef\]](#)
- Blake, W.K. *Mechanics of Flow-Induced Sound and Vibration: General Concepts and Elementary Sources*; Elsevier Science & Technology: San Diego, CA, USA, 2017; Volume 1, p. 300.
- ElMasry, S.; Kühhorn, A.; Figaschewsky, F. Investigation of Working Line Variation onto Forced Response Vibrations of a Compressor Blisk. In Proceedings of the Turbo Expo: Power for Land, Sea, and Air, Virtual, 21–25 September 2020; Volume 84218, p. V10AT24A014. [\[CrossRef\]](#)
- Lin, Y.K. *Probabilistic Theory of Structural Dynamics*; McGraw-Hill: New York, NY, USA, 1967.
- Lutes, L.D.; Sarkani, S. *Stochastic Analysis of Structural and Mechanical Vibrations*; Prentice Hall: Upper Saddle River, NJ, USA, 1997.
- Newland, D.E. *An Introduction to Random Vibrations, Spectral and Wavelet Analysis*, 3rd ed.; Wiley: New York, NY, USA, 1993.
- Meirovitch, L. *Fundamentals of Vibrations*; Waveland Press: Long Grove, IL, USA, 2010.
- Agilis Measurement Systems, Inc. *Non-intrusive Stress Measurement System (NSMS) User Manual*; Agilis Measurement Systems, Inc.: Palm Beach Gardens, FL, USA, 2017.
- Holzinger, F.; Wartzek, F.; Schiffer, H.P.; Leichtfuss, S.; Nestle, M. Self-Excited Blade Vibration Experimentally Investigated in Transonic Compressors: Acoustic Resonance. *J. Turbomach.* **2016**, *138*, 041001. [\[CrossRef\]](#)

28. Welch, P. The use of fast Fourier transform for the estimation of power spectra: A method based on time averaging over short, modified periodograms. *IEEE Trans. Audio Electroacoust.* **1967**, *15*, 70–73. [[CrossRef](#)]
29. Bendat, J.S.; Piersol, A.G. *Random Data: Analysis and Measurement Procedures*; John Wiley & Sons: Hoboken, NJ, USA, 2011.

**Disclaimer/Publisher’s Note:** The statements, opinions and data contained in all publications are solely those of the individual author(s) and contributor(s) and not of MDPI and/or the editor(s). MDPI and/or the editor(s) disclaim responsibility for any injury to people or property resulting from any ideas, methods, instructions or products referred to in the content.